

## ARTICLE OPEN

Moiré-related in-gap states in a twisted MoS<sub>2</sub>/graphite heterojunctionChun-I Lu<sup>1,2</sup>, Christopher J. Butler<sup>1</sup>, Jing-Kai Huang<sup>3</sup>, Yu-Hsun Chu<sup>1</sup>, Hung-Hsiang Yang<sup>1</sup>, Ching-Ming Wei<sup>3</sup>, Lain-Jong Li<sup>3,4</sup> and Minn-Tsong Lin<sup>1,3</sup>

This report presents a series of low-temperature (4.5 K) scanning tunneling microscopy and spectroscopy experimental results on monolayer MoS<sub>2</sub> deposited on highly oriented pyrolytic graphite using chemical vapor deposition. To reveal the detailed connection between atomic morphology and conductivity in twisted MoS<sub>2</sub>/graphite heterojunctions, we employ high-sensitivity tunneling spectroscopy measurements by choosing a reduced tip-sample distance. We discern previously unobserved conductance peaks within the band gap range of MoS<sub>2</sub>, and by comparing the tunneling spectra from MoS<sub>2</sub> grains of varying rotation with respect to the substrate, show that these features have small but non-negligible dependence on the moiré superstructure. Furthermore, within a single moiré supercell, atomically resolved tunneling spectroscopy measurements show that the spectra between the moiré high and low areas are also distinct. These in-gap states are shown to have an energy shift attributed to their local lattice strain, matching corresponding behavior of the conduction band edge, and we therefore infer that these features are intrinsic to the density of states, rather than experimental artifacts, and attribute them to the twisted stacking and local strain energy of the MoS<sub>2</sub>/graphite heterointerface.

npj 2D Materials and Applications (2017)1:24; doi:10.1038/s41699-017-0030-6

## INTRODUCTION

MoS<sub>2</sub> is a semiconducting member of transition metal dichalcogenide family of layered van der Waals materials.<sup>1–4</sup> Monolayer MoS<sub>2</sub> has been shown to be obtainable from the bulk material by micro-exfoliation, similar to the derivation of graphene from the graphite bulk.<sup>5</sup> Such van der Waals 2D materials can be stacked with each other to form vertical heterojunction devices or composite nanomaterials, under the rationale that each layer can be chosen for its distinct electronic properties, which will be retained in the heterostructure.<sup>6</sup>

It is therefore worthwhile to examine the interlayer interactions and their effects on the electronic structure of such 2D interfaces in order to better understand and design advanced heterojunctions. Regarding the basics of interlayer stacking, when two 2D lattices are overlaid, a lattice mismatch and/or an interlayer rotation leads to an additional periodic corrugation called a moiré pattern.<sup>7</sup> The moiré corrugation can behave like a periodic electron localization,<sup>8, 9</sup> giving rise to minibands, quantum well confinement,<sup>10–13</sup> or other phenomena. For example, twisted bilayer graphene can exhibit an overlapping of Dirac cones, forming saddle points and resulting in a van Hove singularity that mediates enhancement of electronic phenomena such as the van der Waals interaction.<sup>14–18</sup> Scanning tunneling microscopy and spectroscopy (STM/STS) are ideal tools for investigating such effects as they can be used to resolve the interaction between morphology and electronic structure at the atomic scale, as has been demonstrated for twisted bilayer graphene.<sup>12, 13, 19–21</sup>

The heterojunction of twisted MoS<sub>2</sub> deposited on graphene or graphite is also noteworthy. The band profile and morphology

have been revealed in previous STM/STS investigations,<sup>22–26</sup> and the opening of a band gap in graphene by overlaying a MoS<sub>2</sub> monolayer has been observed using angle-resolved photoemission spectroscopy.<sup>27, 28</sup> However, the detailed connection between the atomic structure of the twisted heterojunction and the corresponding electronic structure is still lacking. Huang et al. have visualized the moiré patterns clearly, and also shown using STS that the MoS<sub>2</sub> band gap is tunable by the local strain field.<sup>23</sup> But the tunneling spectra from adjacent MoS<sub>2</sub> grains with a relative difference in twisting angle of 18°, and a corresponding difference in moiré patterns, show no significant difference. This is not as expected according to first-principles calculations, which predict that the band structure varies with the rotational angle of the twisted bilayer.<sup>29, 30</sup> We suggest that typical STM set-point parameters as used by Huang et al., such as a current feedback set-point on the order of tens of pico-Amperes and a bias set-point far into the conduction band, chosen to reduce the influence of the tip's electric field,<sup>23, 31</sup> may actually render the measurement insufficiently sensitive to potential moiré related interfacial phenomena. For a further discussion of the effects of different tip-sample distance, we present a series of tunneling spectra by using different set-points in the [Supplementary Information](#). (Please check the [Supplementary Information](#) online for further discussion of the influence of tip-sample distance on the observation of in-gap states).

In this work, we examine the effects of interlayer rotation on the MoS<sub>2</sub>/graphite heterointerface, using STS measurements with increased sensitivity as compared to previous works, and focus on moiré dependent phenomena in the local density of states. In

<sup>1</sup>Department of Physics, National Taiwan University, Taipei 10617, Taiwan; <sup>2</sup>National Synchrotron Radiation Research Center, Hsinchu 30076, Taiwan; <sup>3</sup>Institute of Atomic and Molecular Sciences, Academia Sinica, Taipei 10617, Taiwan and <sup>4</sup>Physical Sciences and Engineering, King Abdullah University of Science and Technology, Thuwal 23955-6900, Saudi Arabia

Correspondence: Minn-Tsong Lin (mtlin@phys.ntu.edu.tw)

Received: 28 December 2016 Revised: 26 April 2017 Accepted: 2 May 2017

Published online: 27 July 2017

order to enhance the sensitivity of the  $dI/dV$  conductance signal, measurements were performed at 4.5 K and with feedback set-points corresponding to a relatively short tip-sample distance. We find small conductance peaks appearing within the original band gap range of MoS<sub>2</sub>, and observe a variation of these peaks' intensity in two adjacent MoS<sub>2</sub> grains with differing moiré patterns. Furthermore, we observe that the peaks shift toward the Fermi level as the measurement position approaches a grain boundary, matching the previously reported shift of the conduction band, which was attributed to a local modification of the strain field. The peak intensities are shown to be distinct between the highs and lows within a moiré supercell, except in the case of large rotation angle, where the peaks have no location dependence, but shift slightly toward the Fermi level. In conclusion, we attribute behavior of these peaks to modification of the heterointerface's electronic structure by variations in the geometric stacking.

## RESULTS

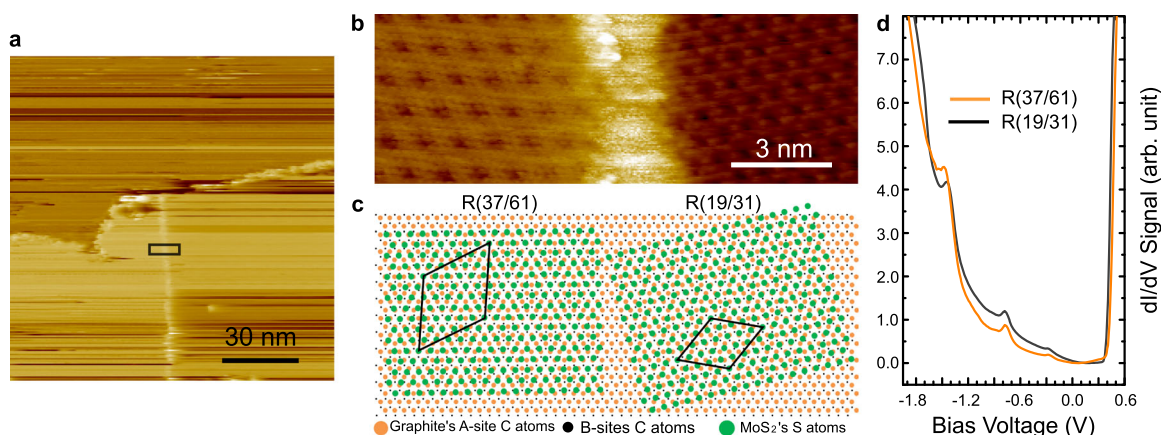
Figure 1a displays the boundary region where two adjacent monolayer MoS<sub>2</sub> grains of different orientations impinge on each other during growth. Figure 1b shows that each of the two grains exhibits a distinct moiré pattern. The image was calibrated by measuring the nearby bare HOPG surface, and moiré period was derived using a 2D fast Fourier transform (FFT). The moiré lattice constant is  $1.11 \pm 0.05$  nm on the left side and  $0.80 \pm 0.05$  nm on the right. The error bar is estimated according to the 2D FFT wavenumber resolution based on the scanning region of  $40 \times 40$  nm<sup>2</sup> with pixel number  $800 \times 800$ . The relative rotational angles between the top layer MoS<sub>2</sub> and the HOPG substrate are  $1^\circ$  and  $14^\circ$  for the left and right grains respectively, derived by measuring the lattice orientation of nearby bare substrate. The schematic diagram of the two grains' twisted stacking are illustrated in Fig. 1c. The supercell periodicities are determined by selecting a point of commensurate stacking (for example, of the S atom above a graphite on-top site, as shown), then shifting a distance to the nearest commensurate point. The supercells are each labeled as a black rhombus in Fig. 1c and are noted as R(37/61) and R(19/31) for the left and right regions, respectively. The notation R(37/61)

denotes that the top MoS<sub>2</sub> unit cell length of 0.315 nm multiplied by  $\sqrt{37}$ , and the bottom graphite unit cell length of 0.246 nm multiplied by  $\sqrt{61}$ , both exactly fulfill the supercell periodicity. The values 37 and 61 are the vector lengths composed by the vectors (4,3) and (5,4) in the hexagonal basis sets of the MoS<sub>2</sub> and graphite lattices.<sup>29, 32</sup> Note that the actual supercell period is not necessarily equal to the apparent moiré pattern's period. Generally, adjacent apparent moiré peaks are seen to have a small difference upon close inspection, and a larger periodicity is necessary for finding another point of exactly commensurate stacking.<sup>24</sup>

We performed a series of STS measurements in the vicinity of this intersection, using a measurement frame of size  $40 \times 8$  nm<sup>2</sup> spanning the boundary. The frame consists of  $200 \times 40$  pixels, each with one tunneling spectrum. Curves acquired on either side of the boundary shared the same physical condition of the tip apex, and the same set-point parameters. Figure 1d presents averaged tunneling spectra obtained in a 85 nm<sup>2</sup> region on each side, each separated by 2 nm from the boundary to avoid edge effects.<sup>22</sup> We observe that the conduction band minimum (CBM) resides at 0.37 V for R(37/61) and at 0.34 V for R(19/31). This supports the experimental results in ref. 22: The formation of a vertical heterojunction between MoS<sub>2</sub> and the graphite represents an extrinsic modification of the MoS<sub>2</sub> CBM value.

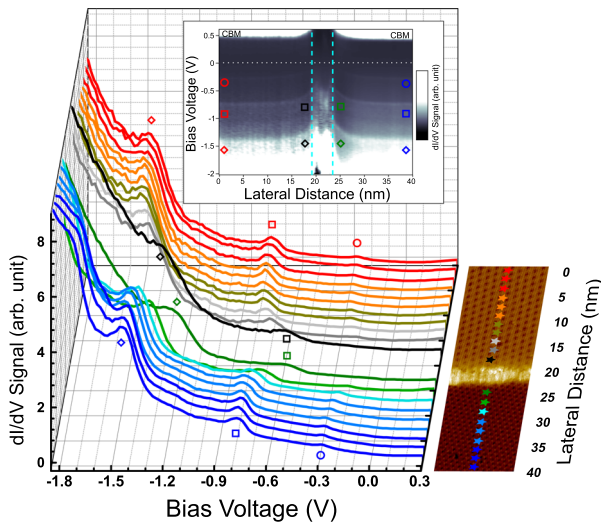
In the negative bias range, peaks appear at  $-0.27$ ,  $-0.78$ , and  $-1.48$  V in the region to the left, and at  $-0.29$ ,  $-0.78$ , and  $-1.44$  V in the region to the right. The valence band maximum (VBM) of MoS<sub>2</sub> has been reported at around  $-1.8$  V,<sup>22, 33</sup> and a substantially shorter tip-sample distance is thought to lead to the apparent difference in the measurements presented here.<sup>31</sup> Qualitatively, we can observe that the peaks appear inside the range normally considered to represent the band gap. The two regions represent identical MoS<sub>2</sub> overlayers covering an identical substrate but with different orientations, and the STS results show the small but not negligible difference in the electronic structure.

Figure 2 presents how these peaks behave near the grain boundary. We analyze the same STS data set of Fig. 1, but arrange the local conductance curves according to their lateral position. Figure 2a displays the tunneling spectra averaged over small regions at selected positions (with centers marked by stars on the



**Fig. 1** Two moiré domains. **a** Large scale STM image ( $V_{\text{bias}} = -0.5$  V,  $I_{\text{set}} = 0.5$  nA) showing the position of the scanning range for **b**. **b** An atomically resolved STM image including two distinct moiré patterns on either side of a boundary ( $V_{\text{bias}} = -0.5$  V,  $I_{\text{set}} = 0.5$  nA). **c** Schematic representations of the two domains with rotational angles of  $1^\circ$  for the left side and  $14^\circ$  for the right side. For clarity, here we only draw the S atoms instead of the complete MoS<sub>2</sub> structure since only the lower S atoms are at the interface, and they occupy the same projected positions as the atomic peaks in the topography image. The superstructures determined for the left and right regions, each indicated by a black rhombus, are R(37/61) and R(19/31), respectively. **d** The averaged STS for the left and right regions. (Set point:  $V_{\text{bias}} = -0.5$  V,  $I_{\text{set}} = 0.5$  nA). The conductivity onset in the conduction band region is located at 0.37 V for R(37/61) and at 0.34 V for R(19/31). In the negative bias range, the peaks appear at  $-0.27$ ,  $-0.78$ , and  $-1.48$  V for R(37/61), and at  $-0.29$ ,  $-0.78$ , and  $-1.44$  V for R(19/31). The tunneling spectra reveal the difference in electronic structure between the R(37/61) and R(19/31) regions

accompanying topography image) along a path crossing the grain boundary, to visualize the position dependence. Each sampling area size is about 5 nm<sup>2</sup> and contains over 100 tunneling spectra. Here we focus on the evolution of the peaks in the negative bias



**Fig. 2** Spatially resolved STS across the grain boundary. (Set point:  $V_{\text{bias}} = -0.5$  V,  $I_{\text{set}} = 0.5$  nA) The upper and lower parts are the R(37/61) and R(19/31) regions, respectively. The spectra show the energy shift of the peaks when the measurement point approaches the boundary. The inset displays the STS line profile. The aqua dashed line labels the boundary of contaminations and the white dashed line labels the Fermi level. The diamonds, squares, and circles represent the three peaks. We observe that the diamonds belonging to the R(19/31) region are shifted from  $-1.46$  V (blue) to  $-1.28$  V (green), and the squares are shifted from  $-0.78$  V move to  $-0.62$  V. For the circles, they shift from  $-0.29$  to  $-0.22$  V, but vanish very near the boundary (deep green curve). In the R(37/61) region, the diamonds are shifted from  $-1.49$  V (red) to  $-1.34$  V (black), and squares from  $-0.78$  to  $-0.64$  V. The circles shift from  $-0.29$  to  $-0.22$  V and also vanish near the boundary (black curve)

range. The inset is the STS line profile which shows the peaks' energy positions move toward the Fermi level and CBM move farther the Fermi level as the position approaches the boundary. According to previous reports, a similar behavior is observed for the CBM and VBM of MoS<sub>2</sub>, and is attributed to the local strain field which can be altered by the grain boundary.<sup>23, 29</sup> In our case, the same tendency can also be inferred for the in-gap peaks. The amount of the shifting reaches 0.16 and 0.21 V for the two lower energy peaks of R(19/31), 0.13 and 0.14 V for R(37/61). Note that the boundary's tunneling spectra are not shown here as such boundaries are covered by contaminations and the spectra are very different from those of the pristine MoS<sub>2</sub> regions. The contaminations are supposed to bond with MoS<sub>2</sub> tightly since MoS<sub>2</sub> has chemically active edges.<sup>34, 35</sup> The adsorbates may shift the absorbents' electronic states due to the charge transfer between each other and that could be detected by STS.<sup>36</sup> However, this kind of influence should be in a short range. For example, the nitrogen-doped epitaxial graphene case shows that the nitrogen influences only the surrounding atoms.<sup>37</sup> In this work, all spectra in this manuscript, were obtained at least 2 nm from the edge in order to avoid the mixed the effects of the contaminations and the lattice strain.

We are also interested in how the electronic structure varies within a single moiré superstructure cell. Figure 3a shows a zoom-in STM topography image of the R(37/61) superstructure region, which is shown at the left side of Fig. 1. The black and red circles label the moiré pattern's higher (H) and lower (L) areas. The line profile in Fig. 3b shows that the apparent height corrugation was measured to be approximately 12 pm. Furthermore, we extracted the tunneling spectra of the R(37/61) area from the STS measurement of Fig. 1, and classified them into two groups: Those from moiré H areas and L areas. In Fig. 3c, each curve is averaged over about 60 spectra from H or L areas. We observe that the shapes of the black and red curves are almost identical except at the two bias voltages  $-1.48$  and  $-0.78$  V, where the peaks of the L areas have a larger signal than those of the H areas. This phenomenon implies that the two states are intimately related to the details of stacking and strain in the moiré structure.

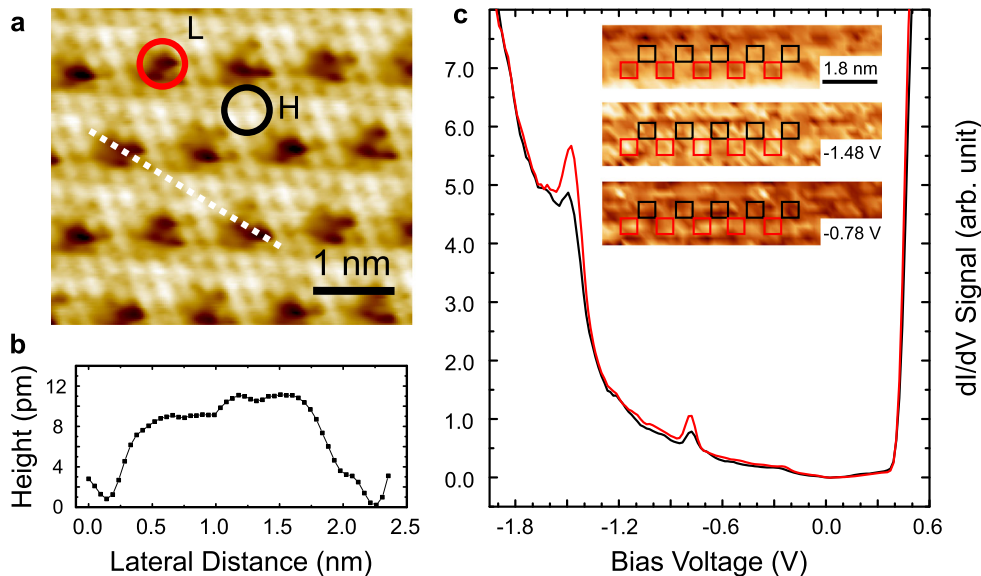


**Fig. 3** Moiré high and moiré low regions. **a** An STM image of the R(37/61) region shown on the left side of Fig. 1 ( $V_{\text{bias}} = -0.5$  V,  $I_{\text{set}} = 0.5$  nA). The black and red circles are label examples of high (H) and low (L) points of the moiré pattern. The dashed white line shows an apparent height corrugation of 12 pm over one period of the moiré pattern. **b** The height profile following the dashed white line. **c** The STS curves averaged over H and L areas are distinct. The red and black curves were averaged from the corresponding rectangular areas shown in the first inset and each rectangle includes around ten spectra. The second and third insets present the  $dI/dV$  conductance mapping at each in-gap peak's energy,  $-1.48$  and  $-0.78$  V. (The spectra are zoom-in of Fig. 2.)

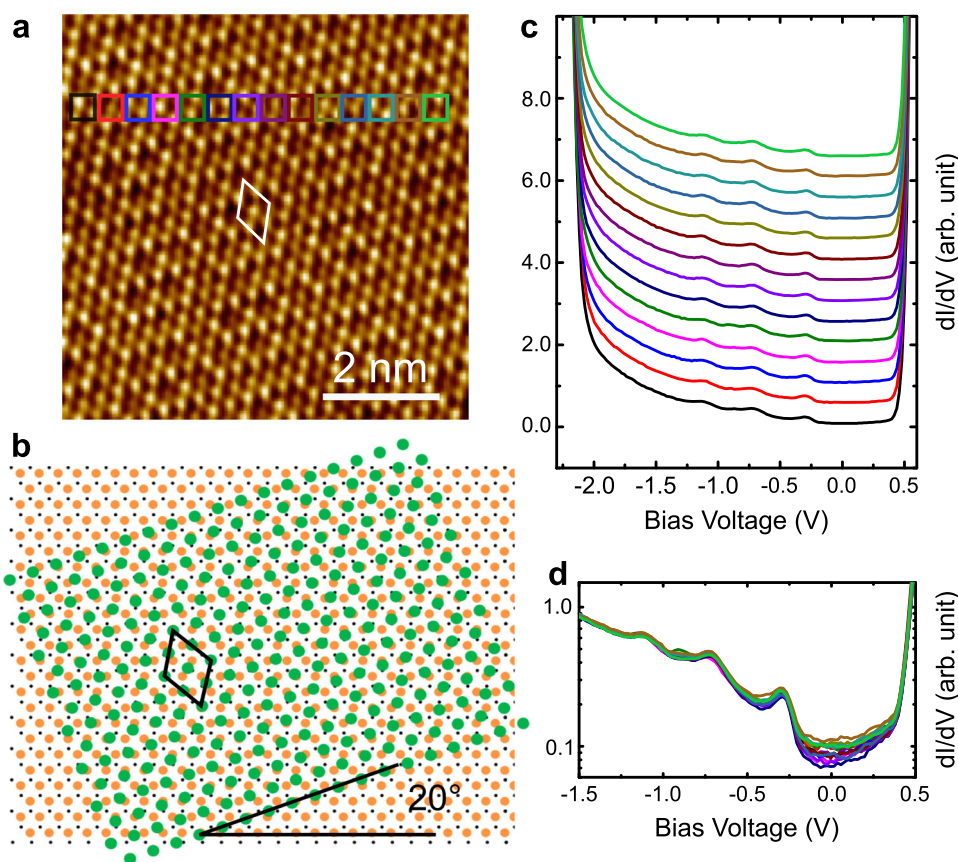


**Fig. 4** Large-angle overlaps. **a** The STM topography of monolayer MoS<sub>2</sub> with a 20° rotation angle with respect to the HOPG substrate (Set point:  $V_{\text{bias}} = -1$  V,  $I_{\text{set}} = 1$  nA). **b** Ball model illustrating the 20° rotated case. The black rhombus labels the moiré superstructure period of the R(4/7) superlattice. **c** The STS curves of the corresponding colored area. The curves are vertically offset for presentation. The set point was:  $V_{\text{bias}} = -1$  V,  $I_{\text{set}} = 1$  nA, and the lock-in modulation was  $V_{\text{mod}} = 30$  mV. **d** The Zoom-in view of the spectra in **c**, with the  $dI/dV$  signal displayed on a logarithmic scale. The peak positions are  $-0.29$ ,  $-0.71$ , and  $-1.11$  V, and the CBM is at  $0.46$  V

Figure 4 presents another case, exhibiting a larger interlayer rotational angle of about 20°, with respect to the lattice of the nearby bare HOPG surface. This case is rare since the rotational angles of CVD grown MoS<sub>2</sub> on HOPG, tend to be small.<sup>23–26</sup> The corresponding ball model is drawn in Fig. 4b. The black rhombus labels the supercell, which is determined in the same way as that shown in Fig. 1c. The supercell period can be composited by an upper sulfur basis with hexagonal vectors (2,0) and (1,2) in the basis of the underlying carbon array. Hence, this case can be labeled as R(4/7). The average over 100 STS curves for each corresponding local area are shown in Fig. 4c. Figure 4d is a further zoom-in view of the band gap region. The peaks appear at  $-0.29$ ,  $-0.71$ , and  $-1.11$  V, and the CBM is at  $0.46$  V. The theoretical band structure of the R(4/7) case has also been investigated by Wang et al. (in which it is denoted as  $\sqrt{7}:4$ ). By comparing the distance between the CBM and the peaks in Fig. 4d and the calculated total density of states in ref. 29, the magnitudes of 1.17 V ( $0.46$  to  $-0.71$  V) and 1.57 V ( $0.46$  to  $-1.11$  V), agree with the values of 1.28 V (CBM to  $\Gamma$  point) and 1.53 V (CBM to K point) in the reference. Also, the small feature in the DFT result, which is in the middle of band gap (below 0.7 V of the CBM), matches our data's first peak which is also below 0.75 V of the CBM ( $0.46$  to  $-0.29$  V) reasonably well. On the other hand, we do not see any position dependence of the tunneling spectra, even in the range of bias near 0 V in Fig. 4d. We suggest this could be explained by the possible decoupling of the top layer from the bottom layer due to the large rotational angle, a phenomenon which is well known in the twisted bilayer graphene system.<sup>12</sup>

## DISCUSSION AND CONCLUSION

As compared to previous STM investigations on the MoS<sub>2</sub>/HOPG system, we use a shorter tip-sample distance to yield increased sensitivity to anticipated moiré dependent phenomena. Such a reduced tip-sample distance could in principle lead to a tip-induced electric field, which plays a critical role in STM measurements on semiconductor surfaces. Dombrowski et al. demonstrated that the tip-induced band bending (TIBB) effect can induce a quantum dot and create new states within the band gap of semiconductors such as InAs during STS measurements.<sup>38</sup> These quantum states were shown to reside within  $-0.1$  V to several tens of mV of the conduction band edge, from which they effectively split off while the tip bias voltage is negative. The states appearing in our measurements are removed from the conduction band edge by a considerably larger margin. Furthermore, although MoS<sub>2</sub> is a semiconductor, the TIBB effect is probably suppressed in the MoS<sub>2</sub>/HOPG system as compared to typical bulk semiconductor materials, due to strong screening from the metallic substrate.<sup>39</sup> Therefore the TIBB effect can not adequately explain our result. The peaks we observe might be attributable to an intrinsic property of the system, rather than an artificial effect of the tip.

The mechanism of observing moiré patterns by using STM does not only involve the top layer, but the process of three-dimensional tunneling, including from buried layers.<sup>40</sup> In our experience, the underlying HOPG substrate can be imaged directly, by using an atypically large set-point current of 50 nA.<sup>24</sup> Thus, not only the surface's information, but also that of the underlying layer can be detected using STM.<sup>31</sup> On the other hand,

first-principles investigations have revealed that there may be a weak but clear charge redistribution in the space between MoS<sub>2</sub> and graphene.<sup>29, 30</sup> In view of the above, we suppose that the newly found peaks are the emergent electronic states associated with the charge distribution in the interlayer space, which can be probed through tunneling channels made accessible by using the shorter tip-sample distance. However, this suggestion can still benefit from further investigation, and to the best of our knowledge, there are, as of yet, no reports focusing on the interlayer charge distribution.

Examining these peaks' bias position, we observe that the three peaks for R(4/7) are shifted toward the Fermi level relative to those discussed above. This implies a relation between the coupling strength between the MoS<sub>2</sub> over-layer and substrate, and the associated lattice strain field, also related to the lattice mismatch. The lattice mismatch between MoS<sub>2</sub> and HOPG can be defined using the simple formula  $f = \frac{a_s - a_e}{a_e}$ , where  $a_s$  and  $a_e$  are the lattice constant of the substrate and the over-layer, respectively.<sup>41</sup> In the MoS<sub>2</sub>/HOPG case, the mismatch is quite large:  $(0.246 - 0.315 \text{ nm}) / 0.315 \text{ nm} = 22\%$ . However, the strain energy could be reduced by skewed stacking the MoS<sub>2</sub> and HOPG. For the 1° rotation case, resulting in a R(37/61) superlattice, the mismatch  $f = (\sqrt{61} \times 0.246 - \sqrt{37} \times 0.315) / \sqrt{37} \times 0.315 = 0.26\%$ . Similarly, for R(19/31),  $f = -0.22\%$  and for R(4/7)  $f = 3.3\%$ .<sup>42</sup> Regarding the conclusion made by Huang et al., the lattice strain energy shifts the VBM toward the Fermi level and the CBM further upwards.<sup>23</sup> In this sense, this could explain why the peak positions of the R(37/61) and R(19/31) cases are similar to each other, but different from the R(4/7) case, due to the strain associated with lattice mismatch.

In conclusion, we discover small previously unobserved in-gap states emerging at the twisted MoS<sub>2</sub>/HOPG heterointerface. These peaks exhibit an energy shift where the lattice strain field changes approaching a grain boundary. Moreover, within a single moiré supercell, the spectra change between moiré high- and low-points. These in-gap states we found are intrinsic, reproducible, and comparable with DFT calculations. With reference to previous theoretical investigations of the MoS<sub>2</sub>/graphene heterojunction, we suggest that these emergent states are intrinsic to the MoS<sub>2</sub>/graphene interface, and may derive from interlayer charges. This finding provides insights for the design of 2D material heterojunctions, highlighting stacking and strain engineering as methods for electronic structure modification.

## METHODS

### Sample preparation

Monolayer MoS<sub>2</sub> islands were prepared on highly oriented pyrolytic graphite (HOPG) using the chemical vapor deposition (CVD) method described previously by Lee et al.<sup>43</sup> The HOPG crystal was purchased from SPI Supplies, 10 × 10 × 2 mm, SPI Grade 1. MoO<sub>3</sub> (99%, Aldrich) and S powder (99.5%, Alfa Aesar) reactants were placed in a nitrogen environment. The MoO<sub>3</sub> powder was reduced to a volatile suboxide MoO<sub>3-x</sub> by the sulfur vapor. The CVD chamber was heated to 650 °C, such that the MoO<sub>3-x</sub> molecules diffused on to the HOPG surface, acquired sulfur atoms from the vapor, and were then deposited on the surface. After deposition in the CVD chamber, the samples were quickly transferred in atmosphere to an ultrahigh-vacuum system for STM measurements. To maintain the thin film's orientation, the sample was directly transferred to the low-temperature STM stage without any heat treatment.

### STM measurements

STM measurements were performed at a temperature of 4.5 K, using an electrochemically etched tungsten tip within commercial LT STM from Scienta Omicron. Atomic lattice unit cells and moiré supercells were determined from atomically resolved STM images as follows: The STM images were calibrated using the ideal HOPG lattice as a reference. The dI/dV spectroscopy signal was derived using the lock-in technique by applying a modulation voltage,  $V_{mod} = 15 \text{ meV}$ , whose

frequency was chosen to be higher than 1 kHz to avoid triggering the feedback loop. The tip was stabilized using a set-point parameters corresponding to a tunnel resistance of 1 GΩ, after which the dI/dV intensity was recorded as a function of bias voltage with the feedback loop open. The energy resolution of dI/dV measurements, determined as the modulation voltage used in the lock-in technique, was 15 mV unless specifically noted otherwise. STM images were processed using the Scanning Probe Image Processor Ver. 4.6.5 and WSxM Ver. 4.0 Beta software packages.<sup>44</sup>

### Data availability

All relevant data are available from the authors. Requests for data and materials should be addressed to M.-T. Lin.

## ACKNOWLEDGEMENTS

This work was supported in part by the Ministry of Science and Technology of Taiwan through grant No. MOST 105-2119-M-002-013.

## AUTHOR CONTRIBUTIONS

C.-I.L. performed STM and STS with assistance from C.J.B., Y.-H.C. and H.-H.Y. The data analysis was performed by C.-I.L. and discussed in depth with C.J.B., Y.-H.C. and M.-T.L. The monolayer MoS<sub>2</sub> was grown by J.-K.H. under supervision of L.-J.L. The theoretical support was provided by C.-M.W. The manuscript was prepared by C.-I.L. and M.-T.L. with assistance from C.J.B. and Y.-H.C. This project was conceived and led by M.-T.L.

## ADDITIONAL INFORMATION

**Supplementary Information** accompanies the paper on the *npj 2D Materials and Applications* website (doi:10.1038/s41699-017-0030-6).

**Competing Interests:** The authors declare no competing financial interests.

**Publisher's note:** Springer Nature remains neutral with regard to jurisdictional claims in published maps and institutional affiliations.

## REFERENCES

1. Bromley, R. A., Murray, R. B. & Yoffe, A. D. The band structure of some transition metal dichalcogenides: III. Group VI A: trigonal prism materials. *J. Phys. C Solid State Phys.* **5**, 759–778 (1972).
2. Böker, T. et al. Band structure of MoS<sub>2</sub>, MoSe<sub>2</sub>, and α-MoTe<sub>2</sub>: Angle-resolved photoelectron spectroscopy and ab initio calculations. *Phys. Rev. B* **64**, 235305 (2001).
3. Coehoorn, R. et al. Electronic structure of MoSe<sub>2</sub>, MoS<sub>2</sub>, and WSe<sub>2</sub>. I. Band-structure calculations and photoelectron spectroscopy. *Phys. Rev. B* **35**, 6195–6202 (1987).
4. Mattheiss, L. F. Band structures of transition-metal-dichalcogenide layer compounds. *Phys. Rev. B* **8**, 3719–3740 (1973).
5. Mak, K. F., Lee, C., Hone, J., Shan, J. & Heinz, T. F. Atomically thin MoS<sub>2</sub>: A new direct-gap semiconductor. *Phys. Rev. Lett.* **105**, 136805 (2010).
6. Geim, A. K. & Grigorieva, I. V. Van der Waals heterostructures. *Nature* **499**, 419–425 (2013).
7. Rong, Z. Y. & Kuiper, P. Electronic effects in scanning tunneling microscopy: Moiré pattern on a graphite surface. *Phys. Rev. B* **48**, 17427–17431 (1993).
8. de Parga, A. L. V. et al. Periodically rippled graphene: Growth and spatially resolved electronic structure. *Phys. Rev. Lett.* **100**, 056807 (2008).
9. Stradi, D. et al. Electron localization in epitaxial graphene on Ru(0001) determined by moiré corrugation. *Phys. Rev. B* **85**, 121404 (2012).
10. Wallbank, J. R., Mucha-Kruczyński, M. & Fal'ko, V. I. Moiré minibands in graphene heterostructures with almost commensurate 3 × 3 hexagonal crystals. *Phys. Rev. B* **88**, 155415 (2013).
11. Bistrizer, R. & MacDonald, A. H. Moiré bands in twisted double-layer graphene. *Proc. Natl. Acad. Sci. USA* **108**, 12233–12237 (2011).
12. Landgraf, W., Shallcross, S., Turschmann, K., Weckbecker, D. & Pankratov, O. Electronic structure of twisted graphene flakes. *Phys. Rev. B* **87**, 075433 (2013).
13. Yin, L.-J. et al. Tuning structures and electronic spectra of graphene layers with tilt grain boundaries. *Phys. Rev. B* **89**, 205410 (2014).
14. Vozmediano, M. A. H., González, J., Guinea, F., Alvarez, J. V. & Valenzuela, B. Properties of electrons near a Van Hove singularity. *J. Phys. Chem. Solids* **63**, 2295–2297 (2002).

15. Dean, C. R. *et al.* Hofstadter's butterfly and the fractal quantum Hall effect in moiré superlattices. *Nature* **497**, 598–602 (2013).
16. Castro Neto, A. H., Guinea, F., Peres, N. M. R., Novoselov, K. S. & Geim, A. K. The electronic properties of graphene. *Rev. Mod. Phys.* **81**, 109–162 (2009).
17. Luican, A. *et al.* Single-layer behavior and its breakdown in twisted graphene layers. *Phys. Rev. Lett.* **106**, 126802 (2011).
18. Lopes Dos Santos, J. M., Peres, N. M. & Castro Neto, A. H. Graphene bilayer with a twist: electronic structure. *Phys. Rev. Lett.* **99**, 256802 (2007).
19. Li, G. *et al.* Observation of Van Hove singularities in twisted graphene layers. *Nat. Phys.* **6**, 109–113 (2010).
20. Zhang, X. & Luo, H. Scanning tunneling spectroscopy studies of angle-dependent van Hove singularities on twisted graphite surface layer. *Appl. Phys. Lett.* **103**, 231602 (2013).
21. Flores, M., Cisternas, E., Correa, J. D. & Vargas, P. Moiré patterns on STM images of graphite induced by rotations of surface and subsurface layers. *Chem. Phys.* **423**, 49–54 (2013).
22. Zhang, C., Johnson, A., Hsu, C.-L., Li, L.-J. & Shih, C.-K. Direct imaging of band profile in single layer MoS<sub>2</sub> on graphite: quasiparticle energy gap, metallic edge states, and edge band bending. *Nano Lett.* **14**, 2443–2447 (2014).
23. Huang, Y. L. *et al.* Bandgap tunability at single-layer molybdenum disulphide grain boundaries. *Nat. Commun.* **6**, 6298 (2015).
24. Lu, C.-I. *et al.* Graphite edge controlled registration of monolayer MoS<sub>2</sub> crystal orientation. *Appl. Phys. Lett.* **106**, 181904 (2015).
25. Liu, X. *et al.* Rotationally commensurate growth of MoS<sub>2</sub> on epitaxial graphene. *ACS Nano* **10**, 1067–1075 (2016).
26. Koós, A. A. *et al.* STM study of the MoS<sub>2</sub> flakes grown on graphite: A model system for atomically clean 2D heterostructure interfaces. *Carbon* **105**, 408–415 (2016).
27. Diaz, H. C. *et al.* Direct observation of interlayer hybridization and Dirac relativistic carriers in graphene/MoS<sub>2</sub> van der Waals heterostructures. *Nano Lett.* **15**, 1135–1140 (2015).
28. Pierucci, D. *et al.* Band alignment and minigaps in monolayer MoS<sub>2</sub>-graphene van der Waals heterostructures. *Nano Lett.* **16**, 4054–4061 (2016).
29. Wang, Z., Chen, Q. & Wang, J. Electronic structure of twisted bilayers of graphene/MoS<sub>2</sub> and MoS<sub>2</sub>/MoS<sub>2</sub>. *J. Phys. Chem. C* **119**, 4752 (2015).
30. Li, X. D. *et al.* Structural and electronic properties of superlattice composed of graphene and monolayer MoS<sub>2</sub>. *J. Phys. Chem. C* **117**, 15347–15353 (2013).
31. Feenstra, R. M. & Stroscio, J. A. Tunneling spectroscopy of the GaAs(110) surface. *J. Vac. Sci. Technol. B* **5**, 923929 (1987).
32. Merino, P., Švec, M., Pinaridi, A. L., Otero, G. & Martin-Gago, J. A. Strain-driven moiré superstructures of epitaxial graphene on transition metal surfaces. *ACS Nano* **5**, 5627–5634 (2011).
33. Chiu, M.-H. *et al.* Determination of band alignment in the single-layer MoS<sub>2</sub>/WSe<sub>2</sub> heterojunction. *Nat. Commun.* **6**, 7666 (2015).
34. Karunadasa, H. I. *et al.* A Molecular MoS<sub>2</sub> edge site mimic for catalytic hydrogen generation. *Science* **335**, 698–702 (2012).
35. Lauritsen, J. V. *et al.* Size-dependent structure of MoS<sub>2</sub> nanocrystals. *Nat. Nanotechnol.* **2**, 53–58 (2007).
36. Yang, H.-H. *et al.* Digitized charge transfer magnitude determined by metal-organic coordination number. *ACS Nano* **7**, 2814–2819 (2013).
37. Joucken, F. *et al.* Localized state and charge transfer in nitrogen-doped graphene. *Phys. Rev. B* **85**, 161408 (R) (2012).
38. Dombrowski, R., Steinebach, C., Wittneven, C., Morgenstern, M. & Wiesendanger, R. Tip-induced band bending by scanning tunneling spectroscopy of the states of the tip-induced quantum dot on InAs(110). *Phys. Rev. B* **59**, 8043–8048 (1999).
39. Ugeda, M. M. *et al.* Giant bandgap renormalization and excitonic effect in a monolayer transition metal dichalcogenide semiconductor. *Nat. Mater.* **13**, 1091–1095 (2014).
40. Kobayashi, K. Moiré pattern in scanning tunneling microscopy: Mechanism in observation of subsurface nanostructures. *Phys. Rev. B* **53**, 11091–11099 (1996).
41. Ayers, J. E., Kujofsa, T., Rago, P. & Raphael, J. *Heteroepitaxy of Semiconductors: Theory, Growth, and Characterization* (CRC press, Boca Raton, FL, 2007).
42. Shen, J., Johnston, S., Shang, S. & Anderson, T. J. Calculated strain energy of hexagonal epitaxial thin films. *J. Cryst. Growth* **240**, 6–13 (2002).
43. Lee, Y.-H. *et al.* Synthesis of large-area MoS<sub>2</sub> atomic layers with chemical vapor deposition. *Adv. Mater.* **24**, 2320–2325 (2012).
44. Horcas, I. *et al.* WSXM: A software for scanning probe microscopy and a tool for nanotechnology. *Rev. Sci. Instrum.* **78**, 013705 (2007).



**Open Access** This article is licensed under a Creative Commons Attribution 4.0 International License, which permits use, sharing, adaptation, distribution and reproduction in any medium or format, as long as you give appropriate credit to the original author(s) and the source, provide a link to the Creative Commons license, and indicate if changes were made. The images or other third party material in this article are included in the article's Creative Commons license, unless indicated otherwise in a credit line to the material. If material is not included in the article's Creative Commons license and your intended use is not permitted by statutory regulation or exceeds the permitted use, you will need to obtain permission directly from the copyright holder. To view a copy of this license, visit <http://creativecommons.org/licenses/by/4.0/>.

© The Author(s) 2017